ARTICLE

Interfacial stability and ionic conductivity enhanced by dopant segregation in eutectic ceramics: the role of Gd segregation in doped CeO_2/CoO and CeO_2/NiO interfaces

Received 00th January 20xx,
Accepted 00th January 20xx

DOI: 10.1039/x0xx00000x

Alodia Orera,[a] Funing Wang,[b,c] Elías Ferreiro-Vila,[d] Sonia Serrano-Zabaleta,[a] Aitor Larrañaga,[e] Miguel A. Laguna-Bercero,[a] Elizabeth C. Dickey,[f] Francisco Rivadulla,[d] M. Carmen Muñoz[b] and Ángel Larrea[a]*

The conductivity of ceramic ionic materials is highly influenced by dopant segregation at the grain boundaries or interfaces, which usually induces a depletion of charge carriers by space charge effects. Hence, obtaining interfacial configurations that promote the formation of oxygen vacancies is highly desirable. In this paper we have combined high resolution electron microscopy (HREM), kelvin probe force microscopy (KPFM) and density functional theory (DFT) to elucidate the equilibrium state of CGO-CoO and CGO-NiO eutectic ceramics (CGO: cerium-gadolinium oxide). HREM proves that the interface is sharp, formed by a single common oxygen plane, and that in CGO-CoO the concentration of gadolinium ions at the interface is almost three times greater than in the bulk, while they distribute homogeneously in the CGO-NiO system. Accordingly, KPFM experiments suggest that interfacial ionic conductivity is much higher in CoO-CGO than in NiO-CGO. DFT demonstrates that Gd segregation in the CGO-CoO reduces the interface energy, contributing to its stability. The Gd-oxygen vacancy complexes compensate the interfacial ionic charge density discontinuity. Additionally, the induced local distortions around the defect release the strain associated with the lattice mismatch. Therefore, we show that in CGO-based eutectics the structure and ionicity of the constituent oxides are essential to promote the interface dopant segregation, indicating a new way to produce nanocomposites with enhanced interfacial ionic conductivity.

Introduction

Dopant segregation to the interfaces and grain boundaries of ionic conductors has a significant influence on the ionic transport of ceramic materials. Grain boundary segregation has been invoked in fluorite-type ionic conductors[1, 2] to explain the observed high grain-boundary resistivity,[3] which is caused by the depletion of oxygen vacancies in the space-charge regions of a negatively charge grain boundary core.[4-8] This type of defect segregation would be detrimental for many technological applications. However, high conductivity has also been reported in sub-micron grains and nanocrystalline samples in acceptor doped ceria[9-12] and an enrichment of mobile oxygen vacancies in the grain boundary or in the interface space charge layer of ion conductors has also been predicted and demonstrated experimentally. [13-18] Moreover, a few mixed phase ionic composites present conductivities higher than those of the bulk phase constituents because of interfacial space charge effects.[19, 20] In general, grain boundary segregation can be driven by strain or size misfit,[R1-R4] as well as by space-charge effects when the dopant has an effective charge as donor or acceptor.[R5-R7] It depends on the doping level, grain boundary crystallography,[21] crystal size[22] or strain conditions[23] and there is no general consensus on the effect of the cation segregation on the oxygen vacancy concentration.[8, 24]

Recently, there has been a growing interest in studying dopant segregation in materials with application in solid oxide fuel cells (SOFC), because of its ability to modify the kinetics of the electrochemical reactions at the electrodes.[25-28] For this type of electrochemical application, directionally solidified eutectic ceramics (DSECs) can serve as model systems to investigate the fundamental mechanisms underlying interfacial dopant segregation in low-energy interfaces, since the interfaces tend to adopt thermodynamically low-energy configurations during the solidification process. However, to our knowledge, dopant segregation in DSEC has not been previously investigated. These materials have self-organized microstructures with large interface densities and they tend to be thermally stable.[29] Combining different constituent phases and microstructures, DSECs with unique properties have been developed for structural,[30-33] photonic[34-37] and energy[38-41] applications, and some DSECs are

[a] Instituto de Ciencia de Materiales de Aragón, CSIC – U. Zaragoza, c/ María de Luna 3, E-50.018 Zaragoza, Spain.
[b] Instituto de Ciencia de Materiales de Madrid, ICMM-CSIC, Cantoblanco, E-28049 Madrid, Spain.
[c] School of Physics, Shandong University, Jinan 250100, China
[d] CiQUS, Centro de Investigación en Química Biolóxica e Materiais Moleculares, Universidade de Santiago de Compostela, Santiago de Compostela 15782, Spain.
[e] SGIker, Servicios Generales de Investigación, Universidad del País Vasco (UPV/EHU), 48080 Bilbao, Spain.
[f] Department of Materials Science & Engineering, North Carolina State University, Raleigh, NC 27695-7907, USA.
E-mail: alarrea@unizar.es
Electronic Supplementary Information (ESI) available. See DOI: 10.1039/x0xx00000x

currently produced by the industry as abrasives.[42] In particular, DSECs formed by ionic conductors and 3*d* transition metal oxides can be used as precursor materials to obtain cermets with applications as energy materials, mainly in the fields of heterogeneous catalysis and solid oxide fuel cells (SOFCs).[43-45]

In this work, we investigate the interfacial configuration in two DSECs made up of an ionic conductor CGO (Cerium Gadolinium Oxide, $Ce_{1-x}Gd_xO_{2-\delta}$) and a 3*d* transition metal oxide, namely CGO-CoO and CGO-NiO, using a combined approach of high-resolution electron microscopy (HREM), density functional theory (DFT) and local kelvin probe force microscopy (KPFM). CoO and NiO have the same crystal structure and almost the same ionicity.[46] However, their lattice parameters are different (a_{CoO}=4.263 Å, a_{NiO}=4.178 Å),[47] which leads to different coherent lattice strain and different ionic charge density imbalance at the interfaces formed with the CGO. Therefore, they provide an interesting platform to elucidate the role of dopant segregation to reduce the electrostatic and lattice misfit at interfaces. We show that in both eutectics the interface is sharp, formed by a single common oxygen plane where the interfacial effects are almost fully confined. However, despite this similarity, the dopant segregation behaviour of the two interfaces is qualitatively different. While Gd segregation, confined to ~1 nm from the interface, reaches a factor of almost 3 with respect to the global concentration in CGO-CoO, no segregation is detected at the CGO-NiO eutectic interface. Moreover, the interface Gd segregation in CGO-CoO is accompanied by the enrichment of oxygen vacancies and, according to preliminary KPFM experiments, by a higher interfacial conductivity. The different behaviour of the two interfaces arises from their different lattice strain and planar charge density misfit. The Gd segregation in CGO-CoO allows the release of the strain associated with the lattice mismatch at the interface and reduces the charge imbalance, leading to lower interface energy. These results open the way to producing bulk nanocomposite materials on an industrial scale with tailored interfacial dopant concentration.

Experiment section

Sample preparation

Samples were prepared by the laser floating zone method (LFZ). The precursors were fabricated from NiO (Grade F, Hart Materials) and CGO ($Ce_{0.9}Gd_{0.1}O_{2-\delta}$) obtained from inorganic salts following the Pechini method.[48] CoO was obtained from Co_3O_4 (99.7%, Alfa Aesar) heated in air at 1000 ºC and subsequently quenched. The powders were mixed (53.86 wt% NiO - 46.14 wt% CGO; 66.36 wt% CoO - 33.64 wt% CGO), isostatically pressed at 200 MPa for 5 minutes and finally sintered at 1400 ºC in air for 2 hours to obtain the cylindrical precursors. Directional solidification was carried out downwards at 100 mm/h using a CO_2 continuous-wave laser with λ=10.6 µm, (Blade 600, Electronic Engineering, Firenze).

Specimen preparation for the TEM experiments

To prepare TEM specimens along the $[100]_{CGO}$// $[1\bar{1}0]_{NiO\text{-}CoO}$ axes, which contain the $(001)_{CGO}$//$(111)_{NiO\text{-}CoO}$ interface,[49] but are generally far from the rod axis, we used an innovative procedure. First, a thick slice of the sample was glued on top of a saw-compatible goniometric stage. Then, this stage was mounted on an X-ray diffractometer to obtain the main pole figures and the orientation angles obtained were translated to the goniometer to align the desired axes to the origin of the Eulerian Cradle. Subsequently, the stage was mounted in a diamond saw to cut a slice with the proper crystallographic orientation. This slice was detached and polished for EBSD, where properly aligned areas were identified. Finally, normal and parallel sections to the polished surface were obtained by focused ion beam (FIB).[50]

For this procedure, X-ray pole figures were obtained using a Bruker D8 Discover diffractometer equipped with Cr tube and a Eulerian Cradle with computer-controlled X–Y–Z stage. Data were collected for three non-equivalent and non-overlapped reflections: (111), (311), and (420) for CGO; (200), (220), and (311) for NiO and CoO. The collection time was 20 s per orientation. The data were acquired in increments of 5° over the range of 0–360° in Phi (φ) and 0–75° in Psi (ψ). Multex 3 software from Bruker AXS was used to calculate the pole figures by component analysis. EBSD experiments were performed in a Carl Zeiss SEM (model Merlin) equipped with a HKL EBSD detector (Oxford Instruments). The orientation maps were obtained using 15 keV, 70° of tilt angle, 800 pA of probe current and 0.2 µm of pixel size. The SEM-FIB procedure was carried out in a Dual Beam FEI Helios 650 using 30 kV Ga^+ ions with 21 nA for the first steps and 5 kV with 40 pA for the final thinning.

X-Ray Diffraction

Lattice parameters for the charge density calculations were determined from powder X-ray diffraction (XRD) in the eutectic samples after grinding to a powder. The experiments were performed using a Rigaku D/max 2500 diffractometer with Cu Kα radiation at 40 kV and 100 mA. Data were collected between 10° and 120° using a step of 0.03° and 3 s per step. The XRD data were refined using the FullPROF Rietveld refinement program.[51]

TEM, EDS and EELS

Energy Dispersive Spectroscopy (EDS) experiments were conducted at North Carolina State University, using a JEOL 2010 scanning transmission electron microscope (STEM) equipped with an EDS detector (Oxford Instruments INCA), and at the National Centre for Electron Microscopy (NCEM, Madrid), using a JEOL 3000F STEM equipped with an Oxford Instruments INCA detector. In order to obtain quantitative results, due to the overlapping of the Gd-Lα^1 (6.059 keV) and Ce-Lγ^1 (6.052 keV) lines and the low level of doping, we acquired 5 spectra of 200 s live time each at different distances from the interface. To ensure no drift, X-ray acquisition was stopped every 30 s and then resumed after manual drift correction when necessary. The spectra were fitted to the Ce-L and Gd-L profiles using the fitting procedures of the INCA® EDS software. The relative Gd/Ce atomic concentration was estimated by the Cliff-Lorimer method[52] using as reference CGO powder previously analysed by Inductive Coupling Plasma (ICP). The error bars were calculated using 1 sigma criterion, considering a Poisson

distribution. Differences in specimen thickness were not considered as EELS experiments confirmed that they were below 2% (see next paragraphs) and also because the X-ray energies of the Ce and Gd characteristic peaks used for the analysis are very similar. Possible differences in thickness between the standard and the analysed specimen were not considered. They would only affect the absolute quantification, not the differences between the bulk and the interfacial region. Moreover, the Gd content obtained in the bulk area of the NiO-CGO sample coincides, within a margin of statistical error, with that of the precursor used, indicating that the EDS quantification procedure is accurate enough.

Atomic resolution STEM-High Angle Annular Dark Field (HAADF) and STEM-Annular Bright Field (ABF) images were acquired using a JEOL ARM200cF aberration-corrected STEM operating at 200 kV. Inner and outer collection semi-angles of 68 and 280 mrad, respectively, for HAADF and 11 and 22 mrad, respectively, for ABF with a nominal camera length of 60 mm were employed. EELS experiments were carried out using a GIF-QuantumERTM with a collection semi-angle of 18 mrad and a convergence semi-angle of 20.3 mrad. EELS data were acquired with a spatial resolution of ~0.08 nm and an energy dispersion of 0.5 eV/channel. EEL spectra were analysed using the Digital Micrograph (DM) software from Gatan. Thickness estimations were done using the log-ratio relative method. The mean free path estimations were obtained using the DM scripts developed by Mitchell & Schaffer.[53]

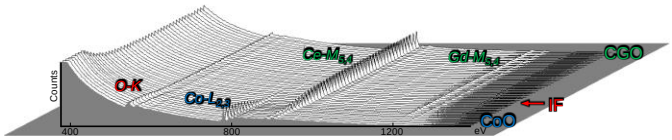

Fig. 1. Line-trace containing the accumulated spectra from all the different regions analyzed. In each pixel we accumulated all the different spectra obtained at the same distance from the interface. The EEL spectra from which the model spectra for the MLLS fittings were obtained are in the top and bottom pixels, for CGO and CoO respectively.

To accumulate enough counts in the EEL spectra without degrading the spatial resolution, spectrum-images from 3 contiguous regions of 100x52 pixel (0.135 nm/pixel) were obtained and all the spectra located at the same distance to the interface were added to obtain a final line-trace for analysis, represented in Fig. 1. In this way, the total accumulated acquisition time at each distance was 6 s and represents a lateral average over a distance of 26 nm, but excluding the steps described afterwards. This process was carried out developing dedicated code in DM scripting language and also using some routines from Mitchell and Schaffer.[53] The difference in thickness between the 3 different regions was less than 2%, the overall estimated thickness being about 85 nm (relative thicknesses are shown in the Supplementary Information, SI)**.** The concentration profiles were calculated by multiple linear least square (MLLS) fitting. The top and bottom pixels of the line-trace were selected as model spectra for the CGO and CoO phases, respectively. The fitting uncertainties were estimated from the σ values calculated by the DM routines using the weighted fitting option based on Poisson counting statistics. As the Poisson uncertainty estimate does not take into account several other uncertainty sources, such as detector noise or fixed patterns in the dark count background, the σ values were corrected by the χ^2_ν factor as explained by Bevington and Robinson[54]. Concentration profiles from EEL spectra were calculated with and without removing plural scattering. The profiles coincide, within the statistical error, because the model spectra were selected from the same spectrum images and, consequently, obtained in areas with the same thickness as the fitted spectra. To minimize mathematical manipulation, the results presented here were calculated without removing plural scattering.

DFT calculations

The density functional theory calculations were performed with the Vienna *ab-initio* simulation package (VASP), which assumes the projector augmented-wave method.[55-58] We have used the generalized gradient approximation (GGA) according to Perdew, Burke and Ernzerhof (PBE) for the exchange correlation functional[59] and a Hubbard U parameter was included to account for the localization of strongly correlated electrons within the rotational invariant approach.[60-62] The $2s^2\ 2p^4$ electrons of oxygen, the $5s^2\ 5p^6\ 6s^2\ 5d^1\ 4f^1$ of cerium and the $5p^6\ 5d^1\ 6s^2$ of Gd, were treated as valence electrons and the Gd $4f^7$ were taken as core electrons. We have also considered the $3s^2\ 3p^6\ 3d^7\ 4s^2$ and $3s^2\ 3p^6\ 3d^8\ 4s^2$ as valence electrons for the Co and Ni magnetic elements, respectively. Values of U=5.1 J=1.0 for Co and U=8.0 J=0.95 for Ni d orbitals were chosen, these being of the same order as those in earlier studies.[63,64] In all the calculations, the plane waves energy cut-off was set to 520 eV, geometries were relaxed employing a conjugate gradient algorithm until the forces on all atoms were less than 0.01 eV/Å and optimizations were performed to self-consistency, with a convergence parameter of 1×10^{-5} eV. The reciprocal space was described by the Monkhorst–Pack scheme.[65]

Kelvin probe force microscopy

AFM measurements were performed on a Park Systems NX10. The experiments were carried out using the Electric Force Microscopy (EFM) mode, which allows the application of a bias voltage between the sample and an electrically conductive AFM tip (Pt-coated, ≈25 nm tip radius) to change the charge density at the surface of the sample. The temporal evolution of the surface electric potential was then monitored with the scanning kelvin probe microscopy (SKPM), with zero bias applied in order to increase the accuracy and resolution of the measurements.[66]

Results and discussion

Microstructure of the interface

The CGO-CoO and CGO-NiO bulk materials are rod-shaped, ~2 mm in diameter and several cm in length (inset Fig. 2a), and formed by ~ 50-100 µm size eutectic grains. The interfacial configuration of DESC materials does correspond to an energy minimum, because minimization of the interfacial energy governs eutectic cooperative

growth.[29] Therefore, inside each eutectic grain the microstructure is lamellar (Fig 2a), the lamellar width (λ) being determined by the competition between the heat flux perpendicular to the growth front and the lateral diffusion. It decreases with the growth rate (v), according to the equation $\lambda^2 \cdot v$=constant.[29] Hence, the typical scale length can be controlled by the processing parameters. In this case, where the samples were grown at 100 mm/h, the interlamellar space was ~700 nm (~200 nm of CGO, ~500 nm of metal oxide), resulting in an interfacial area density of ~$3 \cdot 10^{-6}$ m^{-1}. The lamellae are single crystals with well-defined crystallographic orientation relationships (OR), since they are imposed by the interface with the adjacent phase. The misalignment between the different eutectic grains is small due to the directional solidification and therefore the bulk material is highly textured. The interface alignment of the crystalline planes of the two oxides has been explained by the ionic charge balance at the interface, with the observed planes presenting the lowest ionic charge density misfit.[49] The optimum matching between the ionic charge of the interfacial polar planes is a critical factor in determining the interface in DSECs.[67] However, ionic charge balance can only predict the pair of interfacial planes, but not the particular OR between them, which has been explained by a geometric criterion using a modified coincidence of reciprocal lattice points model (CRLP).[68]

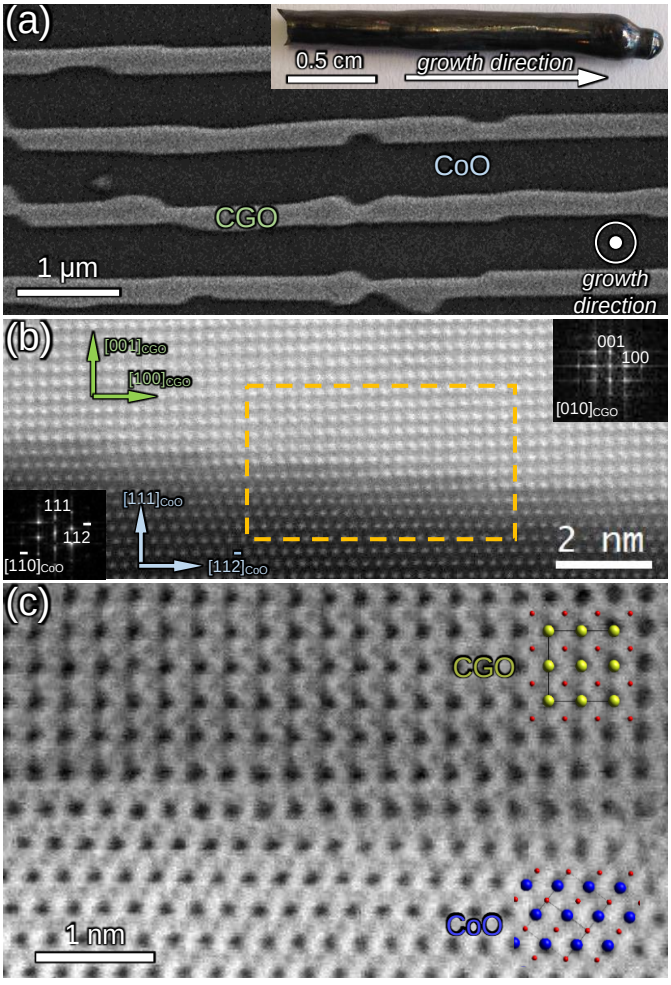

Fig. 2 Microstructure of a CoO-CGO DSEC rod prepared by Laser Floating Zone method at different magnifications. a) SEM image of the transverse cross-section. The inset shows the bulk material. b) HAADF STEM image of the epitaxial CoO-CGO $(001)_{CGO}//(111)_{CoO}$ interface. c) ABF STEM image showing a zoom (orange rectangle) of the interface.

HREM images of the CGO-CoO interface are displayed in Fig. 2b-c. The interface is characterized by the $(001)_{CGO}//(111)_{CoO}$ interfacial planes, while the transverse directions are $[100]_{CGO}//[11\bar{2}]_{CoO}$ and $[010]_{CGO}//[0\bar{1}1]_{CoO}$, consistent with previous results.[49] Similar images of the CGO-NiO composite and details of the electron microscopy specimen preparation and experimental procedures are described in SI section. The interfaces are shown to be stepped, with planar terraces ~2-5 nm in length due to the lattice mismatch along the $[100]_{CGO}//[11\bar{2}]_{CoO}$ directions. Along the terraces, the Ce^{4+} ion rows perpendicular to the interface plane tend to be placed between the two-opposite interfacial Co^{2+} ions, but due to the lattice mismatch this location is no longer stable beyond about ten cations. There should be a step every ~11 atoms in the CGO-CoO and every ~9 atoms in the CGO-NiO, resulting in an angle between the crystallographic plane and the actual interface plane, of ~5° and ~7°, respectively. These values are consistent with TEM observations in different regions and EBSD measurements (see SI). The ABF image (Fig. 2c) shows that the interface is atomically abrupt and between the (001) Ce^{4+} and (111) Co^{2+} planes there is a single common oxygen plane, preserving the cation-anion sequence across the interface. To our knowledge, this is the first direct observation of the interface oxygen plane in DSEC materials. A similar result was inferred from STEM data for ZrO_2-NiO interfaces, but due to the insufficient microscope resolution, the common oxygen plane was not directly imaged.[69] Fig. 3, represents the O-K EEL spectra of the common oxygen interface plane. It shows that the near-edge fine structure is different from those of the two constituent oxides - CoO with a rock-salt structure and octahedral coordination and CGO with fluorite structure and tetrahedral coordination- probably corresponding to a disordered oxygen structure (-see subsequent DFT calculations and SI).

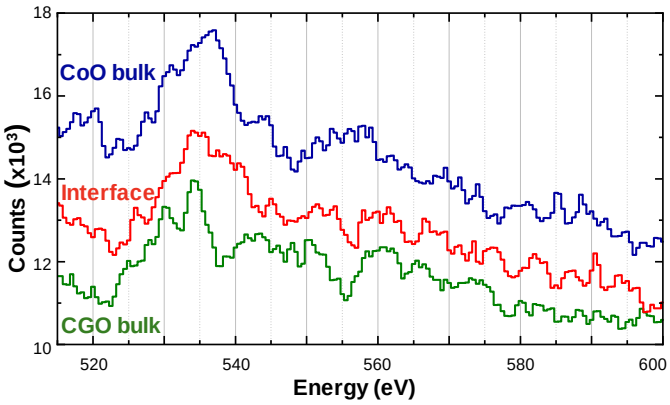

Fig. 3 EEL spectra showing the O-K edge fine structure at the interface and at the two constituent phases.

Gd segregation by EDS and EELS

We measured the Gd distribution across the width of the CGO lamella by energy dispersive X-ray spectroscopy (EDS) with ~5 nm probe size. For the CGO-CoO, the relative intensity of the Gd-Lα^1 peak versus the Ce-L peaks is higher in the spectra taken at the interface than in those obtained in the centre of the CGO lamella (-see SI for representative EDS spectra). Although the difference is not large, we have determined, accumulating 1000 s of acquisition time, that it is 4.8 times higher than its statistical uncertainty, which implies a confidence level higher than 99.9998%. This effect is not observed in the CGO-NiO eutectic. The Gd versus Ce concentration is presented in Fig. 4a. In CGO-NiO it is nearly equal in the centre of the lamella as at the interface. By contrast, the Gd concentration in CGO-CoO is almost constant up to ~10 nm from the interface, where it increases abruptly. The quantitative values, expressed as the *x* parameter in $Ce_{1-x}Gd_xO_{2-\delta}$, are indicated in Fig. 4a. The Gd concentration in CGO-NiO, both in bulk and interfacial zones, corresponds to that of the CGO precursor (x=0.10). However, for the CGO-CoO eutectic, the bulk Gd concentration is lower than in the precursor (x_{bulk} = 0.081±0.003). The extent of the Gd segregation, determined by EELS in the next paragraphs, is not enough to account for the missing GD in the bulk. Therefore we do not have a conclusive explanation for this decrease, although it is probably related to differential evaporation of Gd_2O_3 during the eutectic growth because of the different melting temperatures.

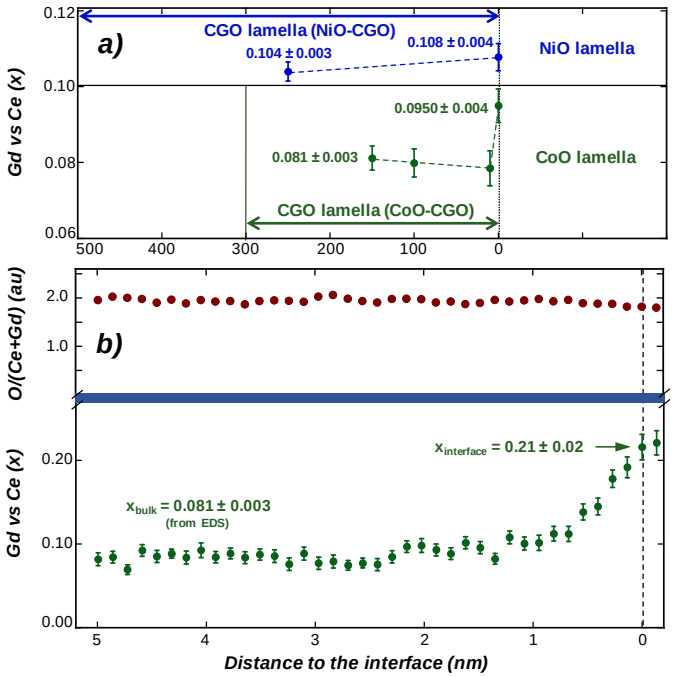

Fig. 4 a) Gd relative concentration from the EDS experiments as a function of the distance to the interface for NiO-CGO and CoO-CGO DSECs (content is expressed as the x parameter in $Ce_{1-x}Gd_xO_{2-\delta}$). The beam spot is about 5 nm in diameter. b) Gd and O relative profiles from the EELS experiments as a function of the distance to the interface. The beam spot is about 0.8 nm in diameter. Error bars indicate only statistical uncertainty.

The Gd concentration determined by EDS corresponds to the mean value in the area activated by the electron beam, ~ 5 nm in diameter. Thus, to ascertain the Gd concentration with atomic resolution we have performed electron energy loss spectroscopy (EELS) measurements in the CGO-CoO samples with a 0.8 nm probe size. EELS data as a function of the distance to the interface does not indicate any change in the oxidation state of the cations. There is no shift in the position of the Co-$L_{2,3}$ edges, demonstrating that the oxidation state of the Co ions remains predominantly 2+ in the interface region. In addition, no changes in the position or relative intensities of the Ce-$M_{5,4}$ edges were found, showing that Ce remains largely 4+.[70] Representative EEL spectra are shown in SI. The Gd ion concentration profile was obtained by multiple linear least square (MLLS) fitting of EEL spectra using background and signal models extracted from spectra obtained in the same eutectic samples several nanometres away from the interface, in the CGO zone for Ce-$M_{5,4}$ and Gd-M_4 edges and in the CoO zone for the Co-$L_{2,3}$ edge (-see SI for the individual profiles). The relative concentration of any two elements can be obtained from the ratio of the integrated intensities over limited energy and angular ranges for particular edges of the elements, divided by the partial scattering cross-section ratio for the same edges and ranges. [71] As the element concentrations away from the interface are known from the EDS experiments, the ratio of the partial cross-sections is directly obtained from EEL spectra taken away from the interface and thus we can scale the integrated intensity ratio to the concentration ratio. The Gd relative concentration in the fluorite phase is presented in Fig. 4b. The concentration is found to be constant up to ~ 5-10 Å from the interface, i.e. about 2-4 atomic planes, increasing up to 2.6±0.2 times the bulk value ($x_{Interface}$ = 0.21±0.02).

The bulk retains the Gd concentration that yields the maximum intragrain conductivity, 8-10 %,[72] whereas at the interface the Gd concentration is very close to the one resulting in the maximum grain boundary conductivity, ~15-20%.[73] Since the ionic conduction is related to the number of mobile oxygen vacancies, it is advisable to determine the variation of the oxygen concentration close to the interface. Therefore, we have estimated by EELS the oxygen profile as a function of the distance to the interface. This is not an easy task because, as previously mentioned, oxygen ions in CoO are in a different environment from CGO, thus affecting the O-K near-edge fine structure in the interfacial region. We have obtained the oxygen profile concentration in the CGO by fitting the O-K fine structure to that of a CGO model spectrum taken away from the interface and comparing this profile with that of Ce plus Gd ions. The oxygen over Ce+Gd ions profile is also represented in Fig. 4b and reveals that the Gd interface segregation is not accompanied in this case by the formation of an oxygen vacancy depleted space charge layer, in agreement with recent predictions.[13-17]. Conversely, the substitution of Gd^{3+} for Ce^{4+} ions is the conventional mechanism for the formation of oxygen vacancies.[72]

Ionic charge balance at the interface has been considered as one of the main requirements for the formation of low-energy interfaces in directionally solidified eutectics since the first phenomenological studies.[67] Eutectic solidification takes place at high temperature and the interface is formed by the diffusion of

high mobility ions from liquid to solid. During solidification, Gd^{3+} ions can be located selectively to reduce the interfacial energy, which mainly depends on the ionic charge configuration at the interface. Considering the formal ionic charges (Co^{2+}, Ni^{2+}, Ce^{2+} and Gd^{3+}) and the lattice parameters determined from powder X-ray diffraction in the investigated samples (a_{NiO}= 4.179 Å, a_{CoO}= 4.258 Å, a_{CGO}= 5.419 Å), the ionic charge densities of the interfacial planes in CGO-CoO and CGO-NiO are:

$\sigma_{(100)-CGO} = \pm 0.266\ e/\text{Å}^2$, for x=0.10

$\sigma_{(111)-NiO} = \pm 0.265\ e/\text{Å}^2$

$\sigma_{(111)-CoO} = \pm 0.255\ e/\text{Å}^2$

Accordingly, for the bulk Gd^{3+} concentration (x=0.10), the ionic charge density balance is very good for the CGO-NiO interface, and therefore differences in the Gd concentration at the interface with respect to the bulk, are not expected, as is confirmed experimentally. Conversely, for the CGO-CoO, the charge density is higher in the $(100)_{CGO}$ than in the $(111)_{CoO}$ planes and the Gd^{3+} concentration in the interfacial $(100)_{CGO}$ plane would increase to reduce the interface mismatch. In fact, a x=0.26 Gd concentration, very close to the x=0.21 experimental value, is required to balance the interface charge density. Therefore, the ionic charge balance provides a good quantitative estimation of the interface Gd content. In addition, the CGO lattice parameter slightly increases with the Gd content, therefore also reducing the lattice strain in the CGO-CoO system.

Density functional theory calculations

Furthermore, the different behaviour of the GCO-CoO and GCO-NiO eutectics is supported by DFT calculations. The bulk structure and electronic properties of the CeO_2, Gd-doped CeO_2, CoO and NiO oxides, as well as additional computational details, are presented in the SI. First, ideal dopant-free $(001)_{CeO2}//(111)_{XO}$ (X=Co, Ni) interfaces were investigated. CeO_2 and XO (X=Co, Ni) are fluorite and rock-salt structures respectively, and both crystallize in the $Fm\bar{3}m$ space group. A two-dimensional (2D) (001) CeO_2 slab is stacked on top of a 2D rock-salt XO slab oriented along the (111) direction and, as observed experimentally, the $[100]_{CeO2}$ and $[11\bar{2}]_{XO}$ crystallographic directions are aligned (-see Fig. 5a-b). Perpendicular to the interface, polar cation and anion planes alternate and therefore the common oxygen plane between the two oxides represents the actual interface. The XO 2D in-plane lattice is commensurate to that of the CeO_2 slab with a c(2x2) fluorite and a c(4x4) rock-salt coincident unit cell. Because of the different symmetry of the (001) fluorite and (111) rock-salt planes, an anisotropic in-plane compressive strain is induced to the transition metal oxides, 8.9 and 3.6 % per unit cell area for CoO and NiO, respectively, the density of oxygen atoms being the same in the fluorite and rock-salt layers.

DFT calculations with periodic boundary conditions were performed for different high-symmetry relative registries between the CeO_2 and the XO oxides. In all cases, independent of the initial location of interface atoms, the atomic coordinates and lattice vector relaxations lead to the most stable configuration, as depicted in Fig. 5a-b, which represent the lowest energy CeO_2-CoO interface structure –in the figure the atomic positions correspond to those obtained in the calculation after relaxation. In agreement with the experimental observations, the interface oxygens are located close to the equilibrium positions of the CoO lattice, (-see Fig. 2c and 5a). Even for registries in which the interface oxygens initially occupy the simple cubic oxygen sublattice of the CeO_2 fluorite, in the relaxed structure they are located close to the equilibrium CoO sites, displayed in Fig. 5. The interface oxygen maintains the three-fold coordination with the nearest Co plane. However, due to their displacement towards the equilibrium positions of the CoO, the Ce-O coordination is different from that of the bulk and there are two inequivalent oxygens, while two oxygens of the interface unit cell are two-fold coordinated with Ce, the other two display one-fold coordination. Therefore, oxygens at the interface plane present some disorder and they are either four or five-fold coordinate, in between the coordination of the bulk CeO_2 and CoO oxides. In addition, interface Ce is seven-fold coordinated and there is a dispersion of Ce-O bond lengths, which ranges from 2.10 to 2.45 Å, but the average Ce-O bond distance (2.30 Å) is analogous to, or even smaller than, the equilibrium Ce-O bond length in CeO_2. Furthermore, due to the inhomogeneous in-plane compressive strain of the CoO slab, the equilibrium interface Co-O bond lengths also vary, 1.96-2.22 Å, and the average bond length is slightly smaller (2.08 Å) than the 2.19 Å of bulk CoO. Consequently, there is a rather strong CeO_2-CoO interface bonding. Fig. 5c displays the coordination of the atoms at the interface. The calculated dissimilar interface coordination of oxygen can explain the different EELS near-edge fine structure observed in the interface O-K spectra of Fig. 3, which is different from those of the two constituent oxides. We would like to point out that the interface structural changes are almost restricted to the interface oxygens and the nearest-neighbour Ce and Co planes.

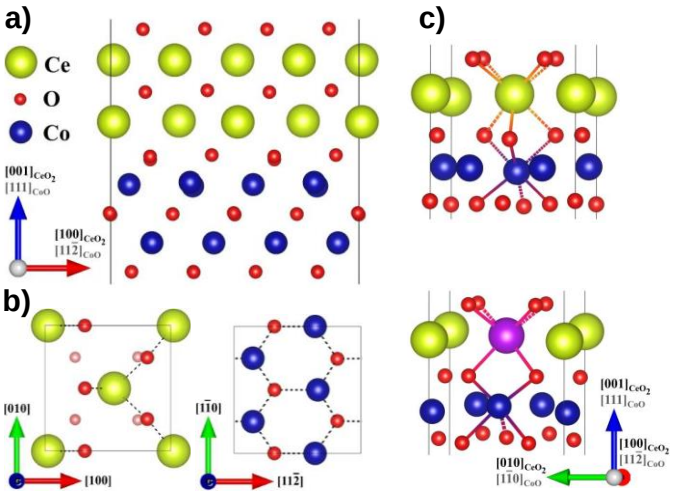

Fig. 5 Lateral (a) and top (b) views of the most stable CoO-CeO_2 interface as obtained from the DFT calculation. The top views only include the two atomic planes (oxygen and metal) closest to the interface, the light red spheres in the Ce-O top view (b) correspond to the ideal oxygen location in the fluorite structure (see text). (c) Representation of the interface bonds illustrating the coordination of the Ce and Co atoms closest to the CeO_2-CoO

interface (top) and of the Gd and Co in the CGO-CoO (bottom).

The equilibrium structure for the CeO_2-NiO interface is analogous with equivalent coordination and 2.30 and 2.05 Å average bond lengths for Ce-O and Ni-O bonds, respectively (-see SI). In terms of energy, we find that both CeO_2-CoO and CeO_2-NiO interfaces are favourable after comparing the total energies of the complete CeO_2-XO slab with the sum of the energies of the isolated CeO_2 and XO slabs. The decrease in energy due to the formation of the interfaces is 487 and 518 meV/A^2 for the CeO_2-CoO and CeO_2-NiO systems, respectively, corresponding to rather strong interfaces.[74-76]

We have analysed the electronic structure of the energetically favourable interfaces. The layer projected density of states (LDOS) shown in Fig. 6 indicates that the CeO_2-CoO system is an electronic insulator since the energy gap is preserved (-see SI). The interface effects are almost restricted to the oxygen plane, while the LDOS in the adjacent Co and Ce layers are very close to those corresponding to the bulk crystals. A significant magnetic moment of 0.36 μ_B is induced in the interface oxygen (0.27 μ_B in the CeO_2-NiO), which also shows an intermediate ionicity in between those of CeO_2 and CoO as measured by the Bader charges.

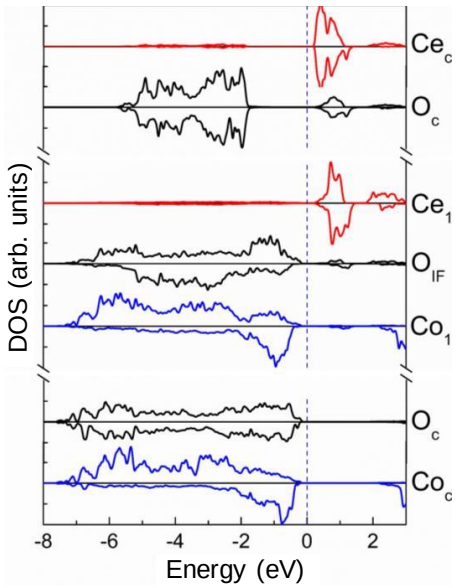

Fig. 6 Spin-resolved density of states projected on the atomic planes around the interface and on two planes in the centre of the CeO_2 (top) and CoO (bottom) slabs. The upper and lower lines within each plane represent, respectively, the majority and minority spin densities. The energy zero is located in the middle of the common gap, so bands with negative energies are occupied and the system is an insulator.

Next we have substituted two gadolinium atoms for cerium and introduced a nearest neighbour oxygen vacancy, V_O, every two Gd cations to model electroneutral CGO (see SI). In order to determine the preferential location of the ($2Gd_{Ce}$-V_O) dopant complex, we calculate CGO-CoO and CGO-NiO superlattices with the dopant complex placed either in the centre of the CGO slab or at the interface, in the latter the V_O being situated at the interface oxygen plane. In both cases, the inclusion of the $2Gd_{Ce}$-V_O complex does not alter the most stable ideal CGO-XO (X=Co, Ni) interface structure. Nevertheless, the bond distances within the planes containing the defects change and the oxygen disorder increases. The effects are larger in the CGO-CoO interface due to the larger in-plane compression stress of the CoO slab.

The most stable structures obtained by DFT are in very good agreement with the high resolution TEM images displayed in Fig. 2c. We define the equilibrium location energy of the dopant complex, E_d^{eq}, as the difference between the energies of the relaxed structures with the dopant complex placed in the center compared to the interface ($E_d^{eq} = E_{d-C}^{rel} - E_{d-IF}^{rel}$). We evaluated E_d^{eq} for the two systems and found 525 and 96 meV per dopant complex for the CGO-CoO and CGO-NiO interfaces, respectively. The large positive CGO-CoO E_d^{eq} unequivocally shows that Gd dopants are preferentially found in the CGO-CoO interface rather than in the bulk, whereas the smaller E_d^{eq} for the CGO-NiO interface indicates that Gd should be randomly distributed in CGO. We have also performed calculations for isolated CGO-XO slabs with two free surfaces, one of CGO and the opposite of XO, and found similar behaviour and an even larger difference between the E_d^{eq} for the two eutectics, (-see SI).

To understand why dopants are preferentially found at the interface in the CGO-CoO and not in the CGO-NiO, despite their equivalent structure and bonding, we analysed the energy associated with the dopant-induced distortions occurring at the interface in both systems. We determined the relaxation energy, defined as the difference in energy between the optimized, E_{d-IF}^{rel}, and unrelaxed, E_{d-IF}^{unrel}, structures, the latter corresponding to the CeO_2-XO system with the substitute $2Gd_{Ce}$-V_O complex before relaxation. The difference is larger in the CGO-CoO than in the CGO-NiO by almost an order of magnitude, 2 and 0.350 eV, respectively, which indicates that the interface relaxation is a key factor in favour of Gd being placed at the CGO-CoO interface. The location of the $2Gd_{Ce}$-V_O complex at the interface allows the interface lattice strain to be relaxed more easily, leading to more stable and lower energy final structures, which is reflected in the large relaxation energies.

Additionally, the LDOS indicates that after Gd doping the interfaces remain electronic insulators, the energy gap being preserved independently of the Gd location -in the bulk or at the interface- and there are neither dopant nor interface-induced gap states. The LDOS at several selected layers for the CGO-CoO and CGO-NiO interfaces are shown in the SI. When the $2Gd_{Ce}$-V_O complex is located at the interface, there are some dopant-induced states in the nearest oxygen, Co and Ni planes, but they are occupied and they do not affect the insulator character of the system. It is interesting to note that interface oxygens have an induced magnetic moment of ~0.2 μ_B and there is a slight reduction of the magnetic moment of the Co and Ni layers.

Calculations with the in-plane lattice parameter of NiO and CoO in which the CGO is under tensile strain were also carried out. They show a smaller interface strength for both systems, although the

qualitative picture is similar. Thus, only calculations with the CeO_2 in-plane lattice parameter have been discussed.

Kelvin probe force microscopy experiments

The ionic conductivity of the interfaces in the CGO-CoO and CGO-NiO eutectics was probed by SKPM. The surface potential of CoO-CGO measured by SKPM is very homogeneous, suggesting good ionic conductivity across the CoO/CGO interface.

To test the charge diffusion across the interfaces, the local concentration of charge carriers was firstly changed by applying a local electric field with a voltage-biased AFM tip. The time evolution of the surface potential was subsequently monitored (at zero electric field) by SKPFM.

Fig. 7 shows the surface potential measured by SKPFM after the initial application of -7 V to a square area of 0.5x0.5 µm. The voltage was applied close to the interface, but mainly in the NiO or CoO region (see white square in the image). The comparison of the KPFM and topographic images shows that, for the CoO-CGO system, there is a strong spreading of the charge along the CGO phase. On the other hand, for the NiO-CGO sample, charge accumulation mostly takes place in the NiO phase, with a much weaker spread through the CGO. These experiments confirm that the ionic conductivity of the CoO-CGO interface is much higher than in NiO-CGO.

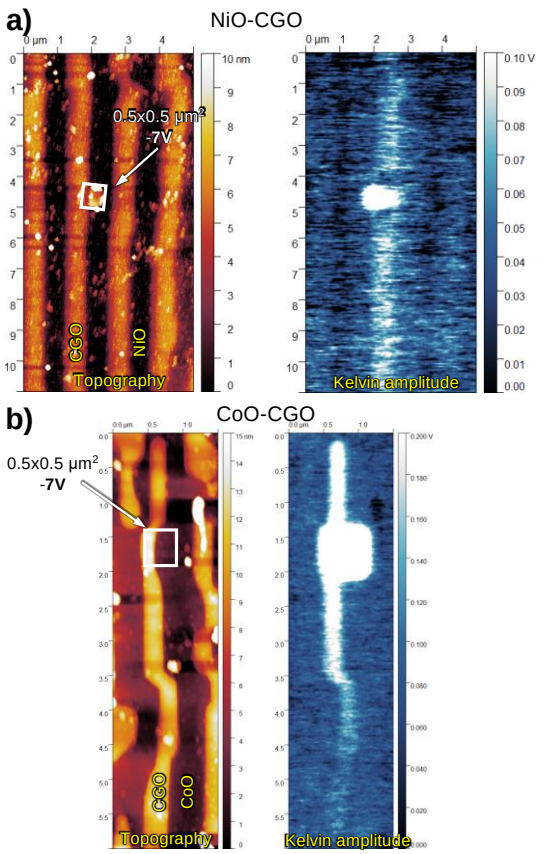

Fig. 7 AFM topographic images (left) and surface potential (right) measured by KPFM on the lamellar microstructure of NIO-CGO (a) and CoO-CGO (b) directionally solidified eutectics. The white square in the topographic images indicates the -7 V polarization zone (0.5 x 0.5 µm). Note that the maximum surface potential of a) and b) are 0.1 and 0.2 V respectively.

We have also performed high-resolution KPFM experiments closer to the CoO-CGO interfaces (Fig. 8). After a few minutes, the diffusion of the charge from the accumulated region to the pristine area is evident. A close inspection of the image shows an enhanced potential along the CoO-CGO interfaces. Therefore, although the contrast of the KPFM signal is not large enough to obtain a completely reliable (and quantitative) conclusion, the results, at least qualitatively, support the hypothesis of a CoO-CGO interface with enhanced ionic conductivity.

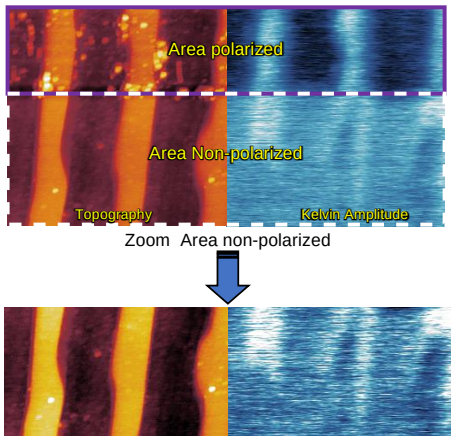

Fig. 8 AFM topographic image 2x2 µm (left) of a CoO-CGO eutectic. The upper area is polarized with 10 V and the surface potential recorded after some minutes (right image).

Conclusions

We have shown that the interface relaxation plays a key role in promoting Gd-segregation at the interface of binary CGO-based eutectics, the structure (lattice parameter) and ionicity (charge density) of the *3d* metal oxide (CoO, NiO) being the essential factors that determine the segregation. Interfaces with a significant lattice mismatch and strong bonding favour Gd-segregation since their energy decreases due to the local distortions induced by the defect. The dopant segregation, accompanied by the enrichment of oxygen vacancies, helps to compensate for the ionic charge density misfit. The formation of a larger number of interfacial oxygen vacancies and the higher disorder of the interfacial oxygen plane, might decrease the activation energy for oxygen migration and, therefore, enhance the interfacial ionic conductivity. In fact, KPFM experiments seem to indicate enhanced interfacial ionic conductivity in the CoO-CGO case. Our results provide a very simple method, by analysing the charge density and lattice misfit imbalance at the interface of two oxides, of anticipating the occurrence of interfacial dopant segregation in ceramic eutectics. Therefore, our findings offer a way of predicting bulk nanocomposite materials with tailored interfacial dopant

segregation, which could be appealing not only for electrochemical, but also for photonic or structural applications.

Conflicts of interest

There are no conflicts to declare.

Acknowledgements

This work was funded through MAT2015-68078-R, MAT2015-66888-C3-1R, MAT2016-80762-R and RTI2018-097895-B-C41 projects by the Spanish Government (Ministerio de Economía y Competitividad) and the Feder Programme of the European Union. Financial support from Xunta de Galicia (Centro singular de investigación de Galicia, accreditation 2016-2019, ED431G/09) is also recognized. F.W. acknowledges the financial support of the China Scholarship Council (CSC) during her stay at the ICMM. A.L. thanks B. Schaffer for his help with Digital Micrograph scripting language and J. Silva for the preparation of ceramic precursors. We are especially grateful to the National Centre for Electron Microscopy (Madrid, Spain), as well as A. Torres-Pardo and Prof. J.M. González-Calbet for their kind assistance and fruitful discussions.

References

1. E. C. Dickey, X. D. Fan and S. J. Pennycook, *J. Am. Ceram. Soc.*, 2001, **84**, 1361.
2. Y. Y. Lei, Y. Ito, N. D. Browning and T. J. Mazanec, *J. Am. Ceram. Soc.*, 2002, **85**, 2359.
3. X. Guo and R. Waser, *Prog. Mater. Sci.*, 2006, **51**, 151.
4. K. Lehovec, *J. Chem. Phys.*, 1953, **21**, 1123.
5. X. Guo, *Solid State Ionics*, 1995, **81**, 235.
6. A. Tschope, *Solid State Ionics*, 2001, **139**, 267.
7. M. C. Gobel, G. Gregori and J. Maier, *Phys. Chem. Chem. Phys.*, 2011, **13**, 10940.
8. B. Feng, N. R. Lugg, A. Kumamoto, Y. Ikuhara and N. Shibata, *Acs Nano*, 2017, **11**, 11376.
9. G. M. Christie and F. P. F. vanBerkel, *Solid State Ionics*, 1996, **83**, 17.
10. C. Y. Tian and S. W. Chan, *Solid State Ionics*, 2000, **134**, 89.
11. T. Suzuki, I. Kosacki and H. U. Anderson, *Solid State Ionics*, 2002, **151**, 111.
12. D. R. Ou, T. Mori, F. Ye, M. Takahashi, J. Zou and J. Drennan, *Acta Mater.*, 2006, **54**, 3737.
13. D. S. Mebane and R. A. De Souza, *Energy & Environ. Sci.*, 2015, **8**, 2935.
14. X. R. Tong and D. S. Mebane, *Solid State Ionics*, 2017, **299**, 78.
15. D. S. D. Gunn, J. A. Purton and S. Metz, *Solid State Ionics*, 2018, **324**, 128.
16. D. V. Laethem, J. Deconinck and A. Hubin, *J. Eur. Ceram. Soc.*, 2019, **39**, 432.
17. G. Sanchez-Santolino, J. Salafranca, S. T. Pantelides, S. J. Pennycook, C. Leon and M. Varela, *Phys. Status Solidi a*, 2018, **215**, 1800349.
18. W. Lee, H. J. Jung, M. H. Lee, Y. B. Kim, J. S. Park, R. Sinclair and F. B. Prinz, *Adv. Funct. Mater.*, 2012, **22**, 965.
19. J. Maier, *Progr. Solid State Chem.*, 1995, **23**, 171.
20. X. X. Guo and J. Maier, *Adv. Funct. Mater.*, 2009, **19**, 96.
21. S. Kim, H. J. Avila-Paredes, S. Z. Wang, C. T. Chen, R. A. De Souza, M. Martin and Z. A. Munir, *Phys. Chem. Chem. Phys.*, 2009, **11**, 3035.
22. P. Knauth, *J. Electroceramics*, 2000, **5**, 111.
23. G. F. Harrington, S. J. Skinner and J. A. Kilner, *J. Am. Ceram. Soc.*, 2018, **101**, 1310.
24. M. A. Frechero, M. Rocci, G. Sanchez-Santolino, A. Kumar, J. Salafranca, R. Schmidt, M. R. Diaz-Guillen, O. J. Dura, A. Rivera-Calzada, R. Mishra, S. Jesse, S. T. Pantelides, S. V. Kalinin, M. Varela, S. J. Pennycook, J. Santamaria and C. Leon, *Sci. Rep.*, 2015, **5**, 17229.
25. Y. Chen, W. Jung, Z. H. Cai, J. J. Kim, H. L. Tuller and B. Yildiz, *Energy & Environ. Sci.*, 2012, **5**, 7979.
26. G. M. Rupp, A. K. Opitz, A. Nenning, A. Limbeck and J. Fleig, *Nature Mater.*, 2017, **16**, 640.
27. Y. Lin, S. M. Fang, D. Su, K. S. Brinkman and F. L. Chen, *Nature Comm.*, 2015, **6**, 6824.
28. S. J. Skinner, *Adv. Mater. Interfaces*, 2019, **6**, 1900580.
29. J. Llorca and V. M. Orera, *Prog. Mater. Sci.*, 2006, **51**, 711.
30. W. T. Chen, R. M. White, T. Goto and E. C. Dickey, *J. Am. Ceram. Soc.*, 2016, **99**, 1837.
31. Y. Waku, N. Nakagawa, T. Wakamoto, H. Ohtsubo, K. Shimizu and Y. Kohtoku, *Nature*, 1997, **389**, 49.
32. P. B. Oliete, J. I. Pena, A. Larrea, V. M. Orera, J. Llorca, J. Y. Pastor, A. Martin and J. Segurado, *Adv. Mater.*, 2007, **19**, 2313.
33. M. C. Mesa, P. B. Oliete and A. Larrea, *J. Cryst. Growth*, 2012, **360**, 119.
34. K. Sadecka, M. Gajc, K. Orlinski, H. B. Surma, A. Klos, I. Jozwik-Biala, K. Sobczak, P. Dluzewski, J. Toudert and D. A. Pawlak, *Adv. Opt. Mater.*, 2015, **3**, 381.
35. Y. Ohashi, N. Yasui, T. Suzuki, M. Watanabe, T. Den, K. Kamada, Y. Yokota and A. Yoshikawa, *J. Eur. Ceram. Soc.*, 2014, **34**, 3849.
36. K. A. A., K. Julia, T. K. I., H. Erik, D.-U. Kim, T. Katsuyo and B. P. V., *Adv. Opt. Mater.*, 2018, 1800071.
37. J. Choi, A. A. Kulkarni, E. Hanson, D. Bacon-Brown, K. Thornton and P. V. Braun, *Adv. Opt. Mater.* 2018, **6**, 1701316.
38. K. Wysmulek, J. Sar, P. Osewski, K. Orlinski, K. Kolodziejak, A. Trenczek-Zajac, M. Radecka and D. A. Pawlak, *Appl. Catal. B-Environ.*, 2017, **206**, 538.
39. M. A. Laguna-Bercero, A. Larrea, J. I. Pena, R. I. Merino and V. M. Orera, *J. Eur. Ceram. Soc.*, 2005, **25**, 1455.
40. L. Ortega-San-Martin, J. Ignacio Pena, A. Larrea, V. Gil and V. M. Orera, *Int. J. Hydrogen Energy*, 2010, **35**, 11499.
41. L. Ortega-San-Martin, J. I. Pena, A. Larrea and V. M. Orera, *J. Eur. Ceram. Soc*, 2011, **31**, 1269.
42. J.R. Quinan, J.E. Parchettt (Norton Company) *US Pat 19730388013,* 1975.
43. M. A. Laguna-Bercero and A. Larrea, *J. Am. Ceram. Soc.*, 2007, **90**, 2954.
44. M. A. Laguna-Bercero, A. Larrea, R. I. Merino, J. I. Pena and V. M. Orera, *J. Am. Ceram. Soc.*, 2005, **88**, 3215.
45. M. A. Laguna-Bercero, A. Larrea, R. I. Merino, J. I. Pena and V. M. Orera, *J. Eur. Ceram. Soc.*, 2008, **28**, 2325.
46. T. Bredow and A. R. Gerson, *Phys. Rev. B*, 2000, **61**, 5194.
47. S. Sasaki, K. Fujino and Y. Takeuchi, *Jpn. Acad. B-Phys.*, 1979, **55**, 43.
48. V. Gil, C. Moure and J. Tartaj, *J. Eur. Ceram. Soc.*, 2007, **27**, 4205.
49. S. Serrano-Zabaleta, M. A. Laguna-Bercero, L. Ortega-San-Martin and A. Larrea, *J. Eur. Ceram. Soc.*, 2014, **34**, 2123.
50. L. A. Giannuzzi and F. A. Stevie, *Micron*, 1999, **30**, 197.
51. J. Rodriguez-Carvajal, *Physica B*, 1993, **192**, 55.

52. G. Cliff and G. W. Lorimer, *J. Microsc.-Oxford*, 1975, **103**, 203.
53. D. R. G. Mitchell and B. Schaffer, *Ultramicroscopy*, 2005, **103**, 319.
54. P. R. Bevington and D. K. Robinson, *Data reduction and Error Analysis for the Physical Sciences*, McGraw-Hill Higher Education, 3rd edn., 2003.
55. G. Kresse and J. Hafner, *Phys. Rev. B*, 1993, **47**, 558.
56. G. Kresse and J. Furthmuller, *Phys. Rev. B*, 1996, **54**, 11169.
57. G. Kresse and D. Joubert, *Phys. Rev. B*, 1999, **59**, 1758.
58. P. E. Blochl, *Phys. Rev. B*, 1994, **50**, 17953.
59. J. P. Perdew, K. Burke and M. Ernzerhof, *Phys. Rev. Lett.*, 1996, **77**, 3865.
60. A. I. Liechtenstein, V. I. Anisimov and J. Zaanen, *Phys. Rev. B*, 1995, **52**, R5467.
61. V. I. Anisimov, F. Aryasetiawan and A. I. Lichtenstein, *J. Phys.-Condens. Mat.*, 1997, **9**, 767.
62. S. L. Dudarev, G. A. Botton, S. Y. Savrasov, C. J. Humphreys and A. P. Sutton, *Phys. Rev. B*, 1998, **57**, 1505-.
63. T. Archer, R. Hanafin and S. Sanvito, *Phys. Rev. B*, 2008, **78**, 014438.
64. H. X. Deng, J. B. Li, S. S. Li, J. B. Xia, A. Walsh and S. H. Wei, *Appl. Phys. Lett.*, 2010, **96**, 162508.
65. H. J. Monkhorst and J. D. Pack, *Phys. Rev. B*, 1976, **13**, 5188.
66. L. Iglesias, A. Gomez, M. Gich and F. Rivadulla, *Acs Appl. Mater. & Interfaces*, 2018, **10**, 35367.
67. W. J. Minford, R. C. Bradt and V. S. Stubican, *J. Am. Ceram. Soc.*, 1979, **62**, 154.
68. S. Serrano-Zabaleta and A. Larrea, *J. Am. Ceram. Soc.*, 2016, **99**, 1015.
69. E. C. Dickey, V. P. Dravid, P. D. Nellist, D. J. Wallis and S. J. Pennycook, *Acta Mater*, 1998, **46**, 1801.
70. J. A. Fortner, E. C. Buck, A. J. G. Ellison and J. K. Bates, *Ultramicroscopy*, 1997, **67**, 77.
71. R. F. Egerton, *Rep. Prog. Phys.*, 2009, **72**, 016502.
72. B. C. H. Steele, *Solid State Ionics*, 2000, **129**, 95.
73. H. J. Avila-Paredes, K. Choi, C. T. Chen and S. Kim, *J. Mater. Chem.*, 2009, **19**, 4837.
74. M. C. Munoz, S. Gallego, J. I. Beltran and J. Cerda, *Surf. Sci. Rep.*, 2006, **61**, 303.
75. M. W. Finnis, *J. Phys.-Condens. Mat.*, 1996, **8**, 5811.
76. J. I. Beltran and M. C. Munoz, *Phys. Rev. B*, 2008, **78**, 245417.